International Journal of Heat and Mass Transfer 52 (2009) 2779–2791

Contents lists available at ScienceDirect

International Journal of Heat and Mass Transfer

journal homepage: www.elsevier.com/locate/ijhmt

Microporous layer for water morphology control in PEMFC

Jin Hyun Nam [a], Kyu-Jin Lee [b], Gi-Suk Hwang [c], Charn-Jung Kim [b], Massoud Kaviany [c,*]

[a] School of Mechanical and Automotive Engineering, Kookmin University, Seoul 136-702, Republic of Korea
[b] School of Mechanical and Aerospace Engineering, Seoul National University, Seoul 151-744, Republic of Korea
[c] Department of Mechanical Engineering, University of Michigan, Ann Arbor, MI 48109, USA

ARTICLE INFO

Article history:
Received 28 May 2008
Received in revised form 4 December 2008
Available online 11 February 2009

Keywords:
Polymer electrolyte membrane fuel cell (PEMFC)
Microporous layer (MPL)
Water management
Catalyst layer (CL)
Catalyst effectiveness
Gas diffusion layer (GDL)
Liquid saturation distribution

ABSTRACT

We have used environmental scanning electron microscope to observe vapor condensation and liquid water morphology and breakthrough in porous layers of polymer electrolyte membrane fuel cell. These suggest presence of large droplets and high liquid saturation at interface of the catalyst layer (CL) and gas diffusion layer (GDL), due to jump in pore size. We develop a model for morphology of liquid phase across multiple porous layers by use of both continuum and breakthrough (percolation) treatments. Using the results of this model we show the liquid morphologies deteriorate the efficiency of electrochemical reactions in CL and increase the water saturation in GDL. Then we show that inserting a microporous layer between CL and GDL reduces both the droplet size and liquid saturation and improves the cell performance.

1. Introduction

Fuel cells are promising energy conversion devices which directly extract electricity from the chemical energy of fuels without resorting to combustion [1–4]. Polymer electrolyte membrane fuel cells (PEMFC) are regarded as clean and efficient power sources for portable, automobile, and residential applications. The low operating temperature (around 70 °C) renders several advantages to PEMFC, enabling fast start-up and good transient characteristics (which are ideal for short-term, repeated operations). However, the low operating temperature also poses several problems, such as the requirement of costly noble metal catalysts for electrochemical reactions and the presence of cumbersome liquid water inside PEMFC.

Water is essential for the operation of PEMFC. PEM, the electrolytes of PEMFC, functions properly when sufficiently hydrated. Thus, fuel and oxidant-gas streams are generally supplied to PEMFC after adequately humidified to avoid dry-out failure of PEM. However, when there is excessive water in PEMFC, the excess water condenses to form liquid which fills the pores in catalyst layer (CL) and gas diffusion layer (GDL), or even blocks gas channel (GC). This phenomenon is called flooding, and is observed in both the anode and the cathode sides of PEMFC. The cathode flooding is caused by continuous generation of water in the cathode CL, and is believed to significantly limit the oxygen diffusion in GDL (as well as the oxygen reduction reaction in CL). The anode flooding also occurs frequently, due to condensation, especially in the PEMFC using pure hydrogen fuel, but has less impact on the cell performance because of the high diffusivity of hydrogen and fast hydrogen oxidation kinetics. On the other hand, the anode water is more difficult to purge and thus presents special challenges for the freeze start-up.

These conflicting effects of water in PEMFC are: a higher water content reduces the ohmic loss because of higher ionic (proton) conductivity in PEM, but also increases the activation and concentration losses because of lower catalyst activity in CL and a lower mass transport rate in GDL. An operating condition that enhances the performance near the inlet of the GC may deteriorate the performance near the outlet. Therefore, the water control in PEMFC has focused on reducing the adverse impacts of liquid water, by devising better flow paths or by optimizing the electrode microstructures. Serpentine and interdigitated flow patterns are the typical examples of such design modifications to obtain better performances by relieving the channel flooding [5,6]. Likewise, microporous layers (MPL) have been successfully used between CL and GDL to reduce the negative effects of the electrode flooding [7–11].

Abbreviations: C, cathode; CL, catalyst layer; GC, gas channel; GDL, gas diffusion layer; MPL, microporous layer; C–D^-, C–D^+, CL–GDL interface: CL side (−) and GDL side (+); C–M^-, C–M^+, CL–MPL interface: CL side (−) and MPL side (+); D–CH, GDL–GC interface: GDL side; M–D^-, M–D^+, MPL–GDL interface: MPL side (−) and GDL side (+).

* Corresponding author. Tel.: +1 734 936 0402; fax: +1 734 647 3170.
E-mail address: kaviany@umich.edu (M. Kaviany).

0017-9310/$ - see front matter © 2009 Elsevier Ltd. All rights reserved.
doi:10.1016/j.ijheatmasstransfer.2009.01.002

Nomenclature

c	mole concentration (mol/m^3)
D_m	diffusion coefficient (m^2/s)
d_{agg}	diameter of catalyst agglomerate particles (m)
F	Faraday number (96,487 C/mol)
$J(S)$	Leverett J-function
j_e	current density (A/m^2)
K	permeability (m^2)
$K(d_p)$	Knudsen factor
L	layer thickness (m)
M	molecular mass (kg/mol)
$\dot{m}$	mass flux (kg/m^2-s)
N_{pb}	number of potential breakthrough pores
n_b	number density for breakthrough pores (m^{-2})
$\dot{n}$	volumetric reaction rate (kg/m^3-s)
p	pressure (Pa)
P_f	flooding probability
R	Universal gas constant (8.314 J/mol-K)
r_d^*	relative droplet size
$\bar{r}_p$	mean pore radius
S	reduced saturation
s	liquid water saturation
s_{im}	immobile saturation

Greek letters

α_d	surface coverage ratio
α_{odp}	net electro-osmosis drag coefficient
β	linear dependence of outlet saturation on liquid water flux (m^2-s/kg)
ε	porosity
Φ	Thiele modulus for diffusion-reaction process
η	overpotential (V)
η_{eff}	effectiveness factor
μ	dynamic viscosity (kg/m-s)
ρ	density (kg/m^3)
θ_c	contact angle (°)
σ	surface tension of water (N/m)

Subscripts and superscripts

b	breakthrough pores
c	capillary
eff	effective values
H_2O	water
l	liquid water
o	reference values
p	pores
pb	potential breakthrough pores

It is generally accepted that MPL provides improved electrical contact between CL and GDL, and helps avoid fast dry-out of PEM at low current densities or low humidity. But, its roles/mechanisms in water PEMFC management, at high current densities or under flooding conditions are not well known. It has been postulated that does by modifying the pore structure of electrodes. Lack of clear understanding is stems from difficulties in observing water transport phenomena inside CL, GDL, and MPL, in operating cells. Recent studies report improved cell performance by modifying microstructure (e.g., porosity, pore size distribution, hydrophobicity, thickness, nonuniformity) of GDL and MPL [7–20]. We note the importance of surface-pore morphologies of MPL recognized in [7]. These experimental results are valuable in investigation of pore-water control in MPL.

Theoretical treatment of the water saturation distribution in GDL is based on continuum two-phase flow models [5,21–27]. The role of MPL in control of water distribution was proposed in treatment of transport in multi-layer electrodes [23,24]. They suggest MPL reduces the water saturation near CL, because of the difference in pore structures of MPL and GDL. They also suggest that a pore-size gradient in multilayer structure improves water transport in the cathode (transport-enhancing role). A different explanation is offered in [25,26], suggesting MPL reduces the cathode flooding by facilitating the back-diffusion of water from cathode to anode (capillary-barrier role). But, recent experimental studies show MPL does not significantly influence this back-diffusion rate [28,29]. In addition, the transport-enhancing role of MPL predicted based on the continuum models, cannot include important pore-level (microscopic) water transport phenomena.

In this study, we propose a new physical model for the roles of MPL in the pore water control in PEMFC. The vapor condensation and liquid water breakthrough in porous layers are observed using environmental scanning electron microscope (ESEM). These, along with the microscopic viewpoint evolved from a recent pore-network analysis on the liquid water transport in GDL [30], are the bases of the physical model. Using existing knowledge about water transport behavior in hydrophobic GDL, the importance of the interfacial water droplets formed between CL and GDL is demonstrated. Then numerical simulations were conducted to assess the limiting effects of these interfacial water droplets on the diffusion rate, the catalyst effectiveness, and the electrochemical reaction rate in CL. We propose two roles of MPL: (a) enhancing the catalyst activity in CL by reducing the size and the saturation level of the interfacial CL–MPL water droplets, and (b) reducing the saturation level in GDL by minimizing the breakthrough number density toward GDL. The structural requirements for MPL to achieve better cell performance are discussed.

2. Experimental observations

Condensation of water vapor inside CL, MPL, and GDL and the subsequent breakthrough of liquid water from these layers were observed using ESEM. In an ESEM, a small amount of water vapor (up to 50 Torr) is allowed in the initially evacuated chamber, and thus a super-saturated condition is achieved by cooling the porous samples to low temperatures (about 4 °C). Thus, water vapor condenses inside pores and this liquid water grows and eventually emerges through the breakthrough pores, as shown in Fig. 1.

Three consecutive CL ESEM images are shown in Fig. 1(a), showing the onset of small water droplet formation at many breakthrough pores and the subsequent growth into larger droplets. These indicate that the surface of the CL is generally hydrophobic, because the water droplets exhibit contact angles larger than 90°. In fact, several microscopic observations have also shown that spherical water droplets are formed on surface of CL [31,32], indicating that CL is generally hydrophobic. This is because of the inclusion of polytetrafluoroethylene (PTFE). Therefore, CL is assumed to be hydrophobic, but has a hydrophilic pore fraction formed by mixing with the PEM material.

ESEM wetting is believed to closely simulate condensation (or generation of water) within CL, and the condensate breakthrough in operating PEMFC, under fully-saturated or flooding condition. In ESEM, vapor condensation is expected to occur primarily within CL, because of its large specific solid–fluid interfacial area as well as cooling from its lower surface in contact with the Peltier cooler. Therefore, most of the water droplets observed in Fig. 1(a) is

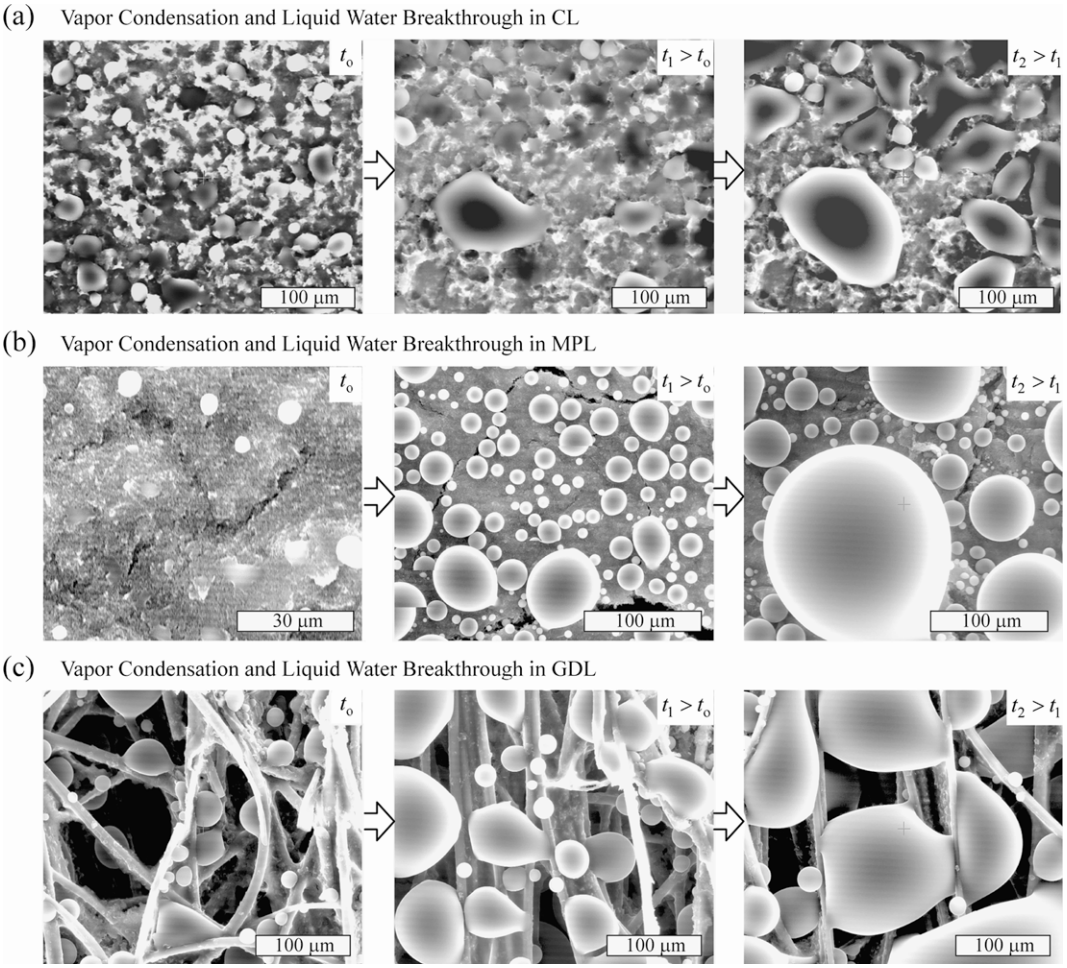

Fig. 1. ESEM micrographs showing vapor condensation and liquid water breakthrough from (a) CL, (b) MPL, and (c) GDL. For each, micrographs at three different elapsed times are shown.

believed to be formed by the breakthrough of liquid water already condensed inside CL. The preferential condensation inside porous samples during ESEM observation is more clearly observable in Fig. 1(c) for GDL, where the specific solid–fluid interfacial area of GDL is much smaller than that of CL.

We note that the number of breakthrough pores from CL is rather large in [Fig. 1(a)]. Increase in internal generation of liquid water increases the number of breakthrough pores from porous layer. The last image in Fig. 1(a) shows that the water droplets can grow very large in large pores. Large droplets formed on CL surface can deteriorate cell performance.

Fig. 1(b) contains ESEM images for MPL, showing the fine pore structure of the MPL. Initially only a few water droplets are observable, but the number increases subsequently, and finally several, very large droplets (larger than 100 μm) are formed by coalescence of smaller water droplets. Fig. 1(b) also shows that MPL is highly hydrophobic, causing formation of nearly spherical water droplets on its surface. In an operating cell, a different water behavior is expected within MPL, because of the expected, limited vapor condensation there. As a result, the MPL number density of breakthrough pores is expected to be smaller than those in Fig. 1(b).

ESEM images for GDL are shown in Fig. 1(c), where the high porosity of GDL and its large pore size allows for close inspection of water morphology changes. Vapor condenses on fibers as large number of small droplets, and these droplets coalesce into larger ones. Finally, very large liquid bodies distorted by the solid structures, are formed and ooze out. Based on similar ESEM observations, a physical model for condensation and condensate transport in GDL (as an inverted tree-like transport structure) was proposed in [23]. In the analysis presented here, the vapor condensation in GDL is assumed to be negligible.

To introduce the MPL to control water, we ask what happens when GDL of in Fig. 1(c) is placed next to CL of Fig. 1(a), as compared to when MPL of Fig. 1(b) to CL? The answer is partly given in Fig. 1. As pointed in [7], the coarse pore structure of GDL allows for growth of large liquid water droplets, but the fine pore structure of MPL will limit their growth. These microscopic water droplet morphologies, at the interfaces, are where our physical model begins.

3. Physical model

3.1. Cathode structure

Structures of cathodes with and without MPL are shown in Fig. 2. PEM is in contact with a thin CL made electrochemically active by mixing with PEM material with additional hydrophobic agent (PTFE), carbon particles, and Pt nanoparticles. In Fig. 2(a), high porosity GDL made of carbon fibers (paper or cloth) with PTFE coating is placed between CL and GC. GDL is a buffer layer for uniform diffusion of reactants and gaseous products. MPL is made of fine carbon particles with PTFE coating and is inserted between CL and GDL, as illustrated in Fig. 2(b), to reduce electrode flooding because of its higher hydrophobicity and smaller pore size

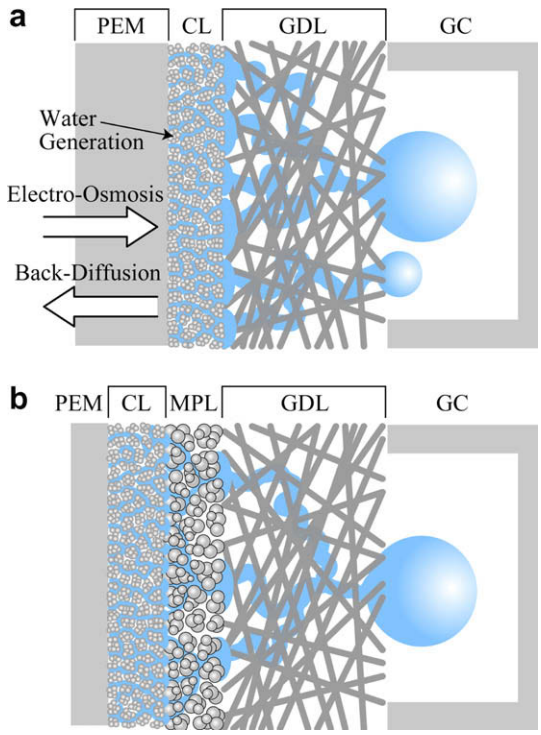

Fig. 2. Structure of cathodes (a) without and (b) with MPL.

compared with GDL. The structural parameters for CL, MPL, and GDL are summarized in Table 1 [33].

The generation and transport of water in cathode are depicted in Fig. 2. Water is produced by electrochemical reaction in CL, and also transported from anode by electro-osmosis drag through PEM. The mass flux of water $\dot{m}_{H_2O}$ in cathode is generally proportional to the current density j_e through

$$\dot{m}_{H_2O} = M_{H_2O}\left(1 + 2\alpha_{odp}\right)\frac{j_e}{2F}, \tag{1}$$

where α_{odp} is the net electro-osmotic drag coefficient (electro-osmosis, back-diffusion, and hydraulic permeation processes through PEM). Fig. 2 shows that this mass flux is transported through porous transport layers (PTL) in the cathode and eventually removed by flow in the GC.

Although not explicitly described in Fig. 2, the vapor phase transport (due to the saturation pressure gradient) can contribute significantly to the total water transport, when the temperature gradient across PTL is large. In [34] the calculated temperature drop across PTL for PEMFC operating at 80 °C and 1 A/cm^2 is estimated as 1–2 °C for GDL Toray carbon papers. Also in [34], a larger drop of around 4–5 °C is predicted for GDL SIGRACET®. We note that the temperature difference of 5 °C corresponds to the saturation pressure difference of about 10 kPa at the operating temperature of 80 °C. Under this condition the vapor transport of water can be significant. However, here we focus on the liquid phase transport of water across PTL by assuming a relatively small temperature drop and small saturation pressure difference.

Table 1
Structural parameters for porous layers in PEMFC.

	CL	MPL	GDL	GC
Porosity ε	20–30%[a]	~50%	70–80%[b]	
Mean pore radius $\bar{r}_p$	~0.05 μm	~0.5 μm	~10 μm	~0.5 mm
Thickness L	10–50 μm	10–100 μm	200–400 μm	

[a] Dry base (swelling of PEM material due to hydration reduces the porosity in CL).
[b] Uncompressed (compression upon assembly reduces the porosity in GDL).

Water transport through GDL has been theoretically treated extensively [5,21–27], since GDL is the thickest layer in PTL, with primary role in homogeneity of reactant-product transport (also has simpler microstructure, compared to CL). In general, GDL is treated as an isotropic and homogeneous porous medium, despite of its layered fibrous structure. The effect of anisotropy on transport properties has been recently shown to be significant [35–37]. For simplicity, here we assume GDL is isotropic.

From a microscopic viewpoint, CL is an inhomogeneous porous medium with randomly distributed hydrophobic and hydrophilic sites. We note that this microscopic inhomogeneity is also found in GDL and MPL. However, CL is generally treated using volume-averaged (macroscopic or masked) models as a homogeneous porous medium with volume-averaged properties. Also, CL is treated as isotropic because of its particle-based structure and the random distribution of its hydrophobic and hydrophilic sites. MPL is also treated as isotropic and homogeneous.

3.2. Water transport in GDL

3.2.1. Water generation in CL

Water flows from CL to GDL as liquid phase under fully-saturated or flooding condition. The catalyst agglomerate models [38–40] treat the solid structure of CL as collection of catalyst agglomerate particles covered with PEM material. The diameter of the agglomerate particles is 1–6 μm (based on experiments) [38,39]. According to such microstructures, thin film of liquid water covers Pt catalyst particles in operating cells, and water is essentially produced as liquid phase.

Whether water is produced as gas or liquid phase is not critical when the specific liquid–gas interfacial area in CL is sufficiently large to enable rapid condensation or evaporation. Then water reaches thermodynamic equilibrium before exiting CL, and the phase of water entering GDL is determined by local conditions near CL. Several studies [23,41] have estimated very large CL specific interfacial area. In addition, the liquid water breakthrough from CL was recently observed in situ [32] in operating cell.

3.2.2. Macroscopic behavior in GDL

Liquid water in GDL tends to exist as droplets or blobs by minimizing its contact with hydrophobic surfaces. If liquid water exists in GDL as spherical droplets, the pressure difference Δp between the liquid p_l and the gas p_g is found from the Laplace–Young equation

$$\Delta p = p_l - p_g = \frac{2\sigma|\cos\theta_c|}{r}, \tag{2}$$

where σ is the surface tension of water (0.0644 N/m at 70 °C), θ_c is the contact angle, and r is the radius of droplet. If r is similar to the mean pore radius listed in Table 1, Δp is estimated about 13 kPa for water droplets in GDL, 260 kPa in MPL, and 2600 kPa in CL, when ideally hydrophobic (θ_c is 180°) pores. From the definition of the mean pore radius, those estimated pressures roughly correspond to the capillary pressure when the water saturation s is about 0.5. For comparison, water droplets in GC have Δp of only about 0.26 kPa when their radii are close to the channel size (0.5 mm).

Liquid water in GDL may not exist as discontinuous droplets, but instead as continuous and complex-shaped liquid bodies with deformed surfaces to fit into the hydrophobic pores. Then, the radius of curvature of liquid surface essentially decreases with water saturation s, due to the limited volume of larger pores in a pore size distribution. In continuum two-phase flow models, this effect is considered by p_c–S correlation, such as the Leverett J-function $J(S)$

$$p_c = p_l - p_g = \frac{\sigma|\cos\theta_c|}{(K/\varepsilon)^{1/2}}J(S). \tag{3}$$

Here, K is the absolute permeability, ε is the porosity, and S is the reduced saturation, defined as

$$S = \frac{s - s_{im}}{1 - s_{im}}. \quad (4)$$

Note that s_{im} denotes the immobile saturation which is the minimum saturation level to secure a continuous liquid phase in a porous medium. Because $J(S)$ is a monotonically increasing function of saturation, the capillary pressure also increases with respect to s.

The transport of liquid water in GDL is because of liquid pressure imbalance between adjacent pores. The gas-phase pressure in GDL is rather constant in steady-state cell operation. Thus, driving force for liquid transport is the capillary pressure gradient caused by nonuniform liquid accumulation in GDL. In continuum two-phase flow models, the liquid mass flux $\dot{m}_l$ uses macroscopic properties such as the relative liquid permeability K_{rl}

$$\dot{m}_l = -\rho_l \frac{KK_{rl}}{\mu_l} \nabla p_c = -\rho_l \frac{KK_{rl}}{\mu_l} \left(\frac{\partial p_c}{\partial S}\right) \nabla S. \quad (5)$$

Note that $(\partial p_c/\partial S)$ term in Eq. (5) is always positive. Then, Eq. (5) indicates that the liquid water in hydrophobic GDL flows from regions of higher saturations towards those of lower saturations. For the relative permeability K_{rl}, a simple correlation is [42]

$$K_{rl}(S) = S^3. \quad (6)$$

Eqs. (3)–(6) describe the liquid transport in GDL and in calculation a set of appropriate boundary conditions are prescribed (such as given mass flux at GDL–CL interface and fixed saturation at GDL–GC interface) to complete the governing equations.

3.2.3. Microscopic behavior in GDL

In microscopic scale, liquid in hydrophobic GDL preferentially chooses larger pores, while flowing toward the GC [23]. Recent pore-network studies show invasion-percolation, which is a strongly capillary-driven process, is an important transport mechanism for the water transport in GDL [30,43]. During invasion-percolation, liquid invades larger pores in random directions because such pores require smaller capillary pressures for liquid water to enter. Recent study [30] also shows the liquid transport paths in GDL are similar to the inverted tree-like structure described in [23]. Many transport paths are formed near CL, due to the rather uniform flux of liquid water entering GDL. Then they converge to several preferential paths of larger pores in the very thin GDL, leading to small number of liquid water breakthroughs from GDL. According to this microscopic behavior of liquid, an effective separation of water-transporting paths (composed of larger flooded pores) and gas-diffusing paths (composed of smaller non-flooded pores) are suggested for hydrophobic GDL. This behavior has been utilized in the optimization of microstructure of GDL and MPL, by introducing bi-modal pore size distributions [15–18].

3.2.4. Liquid breakthrough behavior from GDL

After flowing along preferential paths in larger pores, liquid water emerges from GDL through pores which are much larger than its mean pore size. Upon entering GC, liquid water readily forms spherical droplets attached to GDL and the droplets grow until detached by GC gas flow, as shown in Fig. 2. The water droplets in GC have nearly the same dimension as GC, as solid surface there confines growth of droplets. Thus, GC is viewed as another porous medium with mean pore radius of about 0.5 mm. Then, GDL–GC interface can be considered as an interface of two different porous media.

The continuity of capillary pressure was proposed as the interfacial condition for the water transport in coarse-fine two-layer GDL [23]. This interfacial condition is based on the following observation. When two different porous media with initially the same saturation are brought in contact, the liquid water spontaneously redistributes to form a uniform capillary pressure in the two porous media. According to this argument, liquid water transport in two different porous media inevitably accompanies a saturation jump at the interface to obtain a continuous capillary pressure distribution. However, the continuity of capillary pressure is valid when the pore sizes of two media are similar. And it is difficult to be extrapolated when the pore sizes are widely different. In fact, the pore size of the fine medium considered in [23] was only half of that of the coarse medium.

From a microscopic viewpoint, the capillary pressure may be continuous at the interface of fine-coarse media. However, the macroscopic capillary pressure such as in Eq. (3) used for continuum two-phase flow models cannot be continuous in general. The consequence of this argument is that the water saturation condition in a coarse medium cannot directly influence the water transport in a fine medium located upstream via capillary processes. Thus, the conditions for liquid exiting the fine medium such as the saturation and breakthrough number density are generally independent of the coarse medium.

Liquid water emerging GDL with mean pore radius of about 10 μm encounters 500-μm pores in GC and this large contrast is as if GC is infinitely open. So the liquid water in GC has nearly no influences on water transport in GDL. This is also evident in the wide deference in the capillary pressure levels for GDL and GC, as discussed with Eq. (2). Thus, the boundary conditions at GDL side of GDL–GC interface should be determined by the water transport inside GDL. In many studies, the saturation at GDL–GC interface is assumed constant (around zero or equal to immobile saturation) [21–27]. Here, the saturation just beneath GDL–GC interface s_{D-CH} which depends on GDL pore structure and liquid mass flux is given as

$$s_{D-CH} = f(\dot{m}_l) = s_{im,GDL} + \beta_{GDL}\dot{m}_l. \quad (7)$$

The immobile saturation $s_{im,GDL}$ is the lower bound of s_{D-CH} for small $\dot{m}_l$. The dependence of s_{D-CH} on $\dot{m}_l$ or β_{GDL} is weak, because of the effective separation of water-transporting paths and gas-diffusing paths in hydrophobic GDL.

Note that the water droplets formed in GC cannot directly influence the water transport in GDL through capillary processes, but indirectly by interfering with the diffusion process (thus modifying the electrochemical reaction which governs the local water production in CL).

3.2.5. Breakthrough number from GDL

The value of $s_{im,GDL}$ is generally expected to be 0.1–0.3 (this corresponds to large pore numbers). However, previous studies [44–46] have shown breakthrough of liquid from GDL at very small values of $s_{im,GDL}$ (small pore numbers). The number density of breakthrough pores $n_{b,GDL}$ at GDL–GC interface is dependent on structural parameters of GDL, such as porosity, pore size distribution, as well as liquid mass flux $\dot{m}_l$. However, its minimum may be deduced by the following reasoning. Liquid water introduced from CL invades GDL pores randomly in every direction in search of preferential paths for transport. For isotropic, homogeneous GDL, the invasion front traveled by liquid from a point source at CL–GDL interface must be confined in an expanding hemisphere as shown in Fig. 3(a). Then, the breakthrough of liquid water occurs more frequently near the marked region in Fig. 3(a), where the hemispherical front first touches the GDL–GC interface (directly over the point source).

Consider a straight preferential transport path composed of relatively large pores formed in an otherwise isotropic GDL, as shown in Fig. 3(b). If liquid water from CL finds the preferential path during its random invasion into pores, the liquid water will be

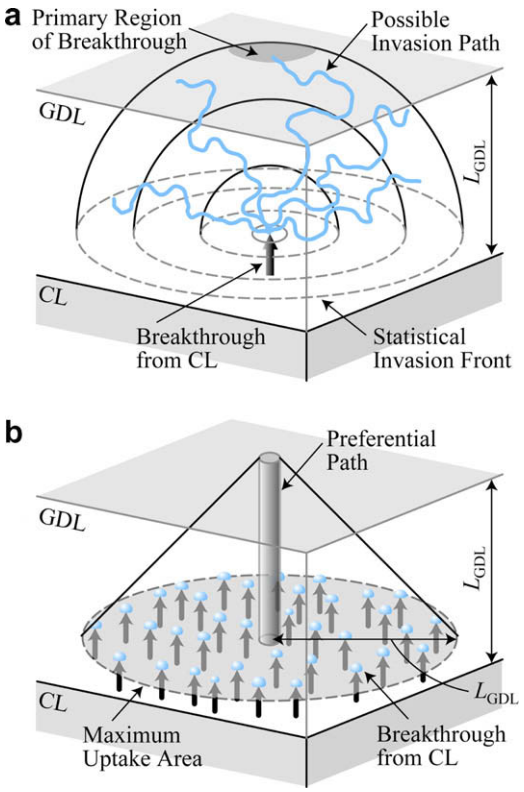

Fig. 3. Breakthrough of liquid water from GDL: (a) formation of spherical invasion fronts, and (b) water uptake by a preferential path.

dominantly transported by that path and emerges from GDL through that surface pore. That is, a preferential path can take up the mass flux of liquid water from a circular area of πL_{GDL}^2 from CL under ideal case. Thus, the minimum number density (per unit area) of the breakthrough pores from GDL is estimated as

$$N_{b,GDL}^{min} = \frac{1}{\pi L_{GDL}^2}, \tag{8}$$

provided that the liquid flux from CL is uniform. According to Eq. (8), a minimum of about 5–6 breakthrough pores per mm^2 is estimated for GDL with L_{GDL} = 250 μm. Several images of water droplet formation in GC show similar breakthrough number densities from GDL [46]. Note that $n_{b,GDL}$ is highly dependent on L_{GDL}.

GDL is not isotropic (layered fibrous structures) and its transport properties such as conductivity, diffusivity, and permeability, are generally larger for the in-plane direction than the cross-plane direction [35–37]. If such trend holds for the liquid water transport in GDL, a preferential path can take up water flux from a larger area of CL, and the number density of breakthrough pores may become smaller.

3.3. Role of MPL

3.3.1. Breakthrough behavior from CL

The water transport behavior in CL is similar to GDL, except liquid water is produced internally. The water generation rate is believed rather uniform inside CL, because of high activation overpotential of the cathode electrochemical reaction. Experiments show that CL pores are hydrophobic with some hydrophilic pores created by inclusion of PEM material [47–49]. Then, the breakthrough of liquid water from CL is possible when capillary pressure becomes positive through accumulation of water over the hydrophilic portion of pores. This behavior can be incorporated into continuum two-phase flow models, by adjusting the immobile saturation s_{im} to include both the percolation threshold and the hydrophilic pore fraction [25,49].

Breakthrough of liquid from CL is similar to GDL and this analogy is shown in Fig. 4, where a water droplet formed at CL–GDL interface and one at GDL–GC interface, are compared. For liquid emerging from CL (mean pore radius of 0.05 μm), the 10-μm mean radius in GDL appear infinitely large. Upon exiting CL, liquid water forms droplets attached to CL and grows thus filling the pores of GDL. Here, we use 'interfacial water droplets' to denote water droplets formed in the coarse medium (at an interface between fine-coarse media). The size of interfacial water droplets is naturally determined by the coarse medium pore size. Thus, typical radius of the interfacial water droplets formed at CL–GDL interface corresponds to the mean pore radius of GDL, although deformed by fibrous structures.

Considering the capillary pressure level in GDL is much lower than that in CL, the continuity of capillary pressure is difficult to achieve at CL–GDL interface, the same as at GDL–GC interface. The microscopic capillary pressure may be continuous near the breakthrough locations, but the macroscopic capillary pressure cannot generally be continuous there. Thus, the water saturation or capillary pressure condition in GDL has less influence on liquid transport in CL located upstream. The water saturation at CL side of CL–GDL interface s_{C-D^-}, is determined only by pore structure of CL and liquid water flux $\dot{m}_l$, similar to Eq. (7), as

$$s_{C-D^-} = f(\dot{m}_l) = s_{im,CL} + \beta_{CL}\dot{m}_l. \tag{9}$$

In general, $s_{im,CL}$ is larger than $s_{im,GDL}$ due to the presence of hydrophilic pores in CL. In addition, β_{CL} is expected to be larger than β_{GDL}, because of the uniform generation of water within CL.

Note that these interfacial water droplets formed at CL–GDL interface cannot directly influence the water transport in the CL by capillary processes. However, their indirect influence on liquid transport by hindering diffusion process can be significant (be-

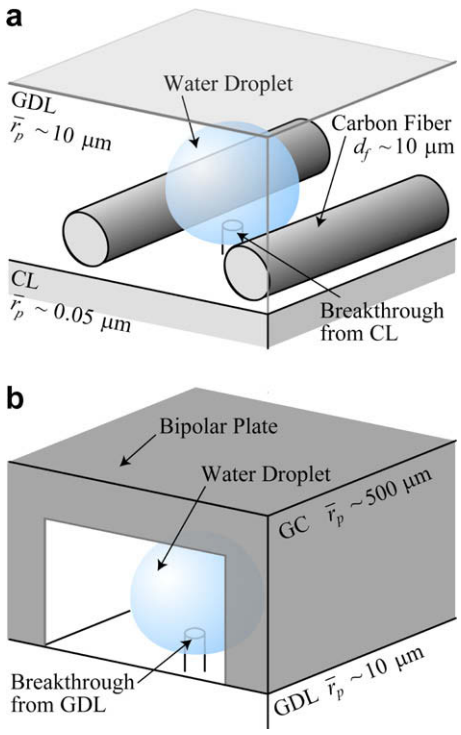

Fig. 4. Geometrical analogy between (a) breakthrough of liquid water from GDL, and (b) that from CL.

cause of the relatively large size of interfacial water droplets and the proximity of droplets and catalyst particles in CL).

3.3.2. Breakthrough number from CL

The number density of breakthrough pores at CL–GDL interface is important, because it constitutes the inlet condition for the water transport in GDL. However, the geometrical argument developed to estimate the number density of breakthrough pores from GDL in Eq. (8) cannot be applied to CL. This is because water is generated rather uniformly inside CL according to reaction and transport there. As shown in Fig. 5(a), the region in CL adjacent to CL–GDL interface also produces a considerable amount of liquid water. That product liquid is less probable in long-distance transport along preferential paths in Fig. 5(a). Instead, it flows directly toward CL–GDL interface and emerges from CL through another breakthrough pore. Thus, the number density of breakthrough pores $n_{b,CL}$ at CL–GDL interface is much larger than $n_{b,GDL}$ at GDL–GC interface. In addition, $n_{b,CL}$ does not significantly depend on the thickness of CL, but depends more on water generation rate in CL.

Based on the catalyst agglomerate models [38–40], a surface layer of CL is assumed to be made of catalyst agglomerate particles arranged as square lattice, as shown in Fig. 5(b). Potential breakthrough pores are then formed in the interstitial space among the surface agglomerate particles and their number density $n_{pb,CL}$ is estimated as

$$N_{pb,CL} = 1/d_{agg}^2. \tag{10}$$

Assuming the mean diameter of agglomerate particles d_{agg} is 3 μm [38–40], the number density of potential breakthrough pores $n_{pb,CL}$ is estimated to be about 1/9 μm^{-2}. Liquid water produced by an agglomerate particle in the surface layer, such as the one in the center of Fig. 5(b), can choose a preferential breakthrough pore among the four potential breakthrough pores marked as A. That is, the potential breakthrough pores have the flooding probability P_f^o of 25% and this corresponds to $n_{b,CL}$ of 1/36 μm^{-2}, or about 27,000 breakthrough pores per mm^2.

Considering microscopic configuration of PEM material in CL, water transport among agglomerate particles through PEM material may be possible for a short distance. If liquid from an agglomerate particle can move rather easily to the nearest neighbor agglomerate particles, it can choose where to emerge out of CL from total of 12 potential breakthrough pores marked as A and B. In this case, the flooding probability is about 8%, which is correspondent to $n_{b,CL}$ of 1/108 μm^{-2}, or about 9000 breakthrough pores per mm^2. If liquid can move further for two agglomerate particle distances rather easily, total of 24 potential breakthrough pores marked as A, B and C are available with flooding probability P_f^o of about 4%. This corresponds to $n_{b,CL}$ of 1/216 μm^{-2}, or about 4500 breakthrough pores per mm^2. Recently, in situ observation of water droplet formation on CL surface was reported [32]. Inspection of these microscopic images, gives a breakthrough number density $n_{b,CL}$ of 1/500 μm^{-2}. However, it should be noted that very small droplets are difficult to observe, and thus the actual breakthrough number density from CL can be larger than this estimate.

Another implication of the production and transport roles of CL is that an effective separation of water-transporting paths and gas-diffusing paths is more difficult to be achieved in CL than in GDL. A region in CL with less liquid near gas-diffusing paths is generally more active in electrochemical reactions than the remaining regions (due to a higher diffusion rate). However, more current generation in that region inevitably accompanies more water production, which in turn leads to increase in local saturation level there. Thus, time-stable liquid–gas interfaces are more difficult to achieve in CL. This process of saturation equalization can gradually amplify and significantly degrade the cell performance.

3.3.3. Interfacial water droplets at CL–GDL interface

The number density of breakthrough pores from CL has not been measured due to experimental difficulties. However, recent experimental study [32] shows the possibility of observing and counting water droplets emerging from CL in operating cells. Here, a statistical approach based on a changeable flooding probability P_f^o is adopted to estimate the saturation level of the interfacial water droplets formed at CL–GDL interface. Fig. 6 illustrates a network of pores at CL–GDL interface, where small potential breakthrough pores in CL are connected to a large pore in GDL. The number of potential breakthrough pores connected to the large pore in GDL is proportional to cross-sectional area of the large pore formed at CL–GDL interface. Assuming the flooding probability P_f^o is constant for all potential breakthrough pores in CL, the flooding probability of the large pore in GDL can be expressed as a function of the number of potential breakthrough pores N_{pb} as

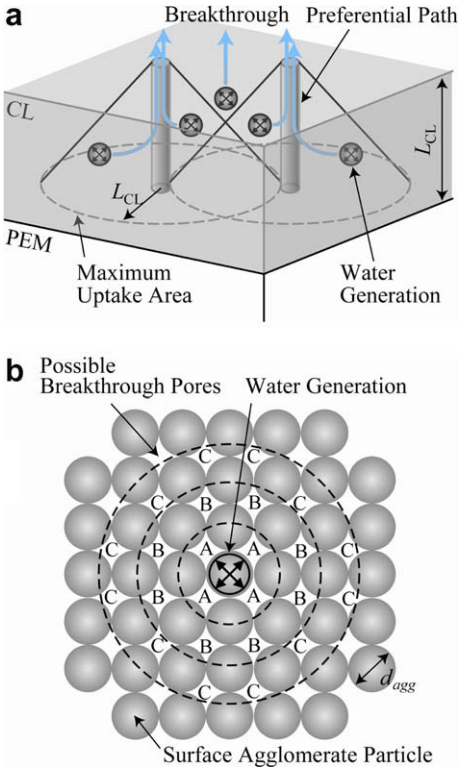

Fig. 5. Breakthrough of liquid water from CL: (a) effect of distributed water generation, and (b) surface layer with arranged agglomerate particles.

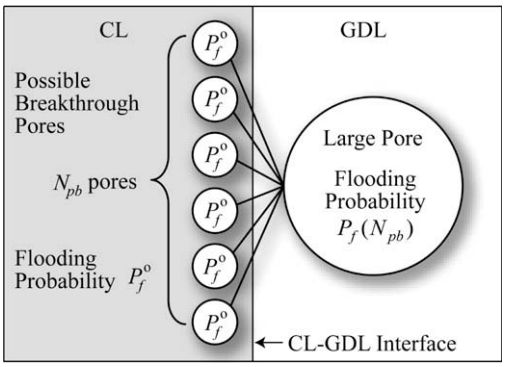

Fig. 6. Pore connectivity of small pores in CL and a large pore in GDL.

$$P_f(N_{pb}) = 1 - \left(1 - P_f^o\right)^{N_{pb}}. \quad (11)$$

The flooding probability in Eq. (11) was derived from the fact that a large pore in GDL is not flooded only when all potential breakthrough pores connected to it do not exhaust liquid water. The result of Eq. (11) in terms of N_{pb} is plotted in Fig. 7(a), where the flooding probability for large pores in GDL $P_f(N_{pb})$ increases with N_{pb} as expected. The flooding probability reaches almost 100% when $N_{pb} > 100$, irrespective of the source-side flooding probability P_f^o considered here. The effect of pore radius in GDL can be studied by converting $P_f(N_{pb})$ into $P_f(r_p)$ as

$$P_f(r_p) = 1 - \left(1 - P_f^o\right)^{\pi r_p^2 n_{pb,CL}}, \quad (12)$$

where r_p is the radius of pores in GDL, and $n_{pb,CL}$ is the number density of potential breakthrough pores from CL in Eq. (10), assumed to be 1/9 μm^{-2}.

Fig. 7(b) clearly shows that saturation level of interfacial water droplets at CL–GDL interface is significantly higher than that at CL–MPL interface. Large pores have much higher flooding probability than smaller ones, because their cross-sectional area is determined as πr_p^2. The cross-sectional area is in fact the compartmental area formed on surface of CL due to solid structure of coarse medium, which is GDL or MPL. In Fig. 7(b) pores in GDL larger than 20 μm in radius become almost always flooded, irrespective of P_f^o. By combining the flooding probability $P_f(r_p)$ and the pore size distribution of GDL especially near the interface, the surface coverage α_d on surface of CL or the saturation level at GDL side of CL–GDL interface s_{C-D^+} may be estimated.

The microscopic configuration of interfacial droplets at CL–GDL interface and that at CL–MPL interface are illustrated in Fig. 8(a) and (b). The pores in GDL at CL–GDL interface are relatively large due to its high porosity and large fiber radius (5 μm). However, the pores in MPL at CL–MPL interface are small (around its mean particle radius of an order of 1 μm). If the same numbers of breakthrough pores are randomly formed at CL–GDL and CL–MPL interface, as represented as small dots in Fig. 8(a) and (b), drastically different interfacial water droplets are formed. The first role of MPL is clearly identified by comparing Fig. 8(a) and (b). The interfacial water droplets formed at CL–GDL interface are large (comparable to CL thickness) with high saturation level, which result in reduced open area toward CL. This leads to a significant reduction of the diffusion and reaction rates in CL. By inserting MPL, the size and saturation level of the interfacial droplets on surface of CL is significantly decreased, leading to an improved water management.

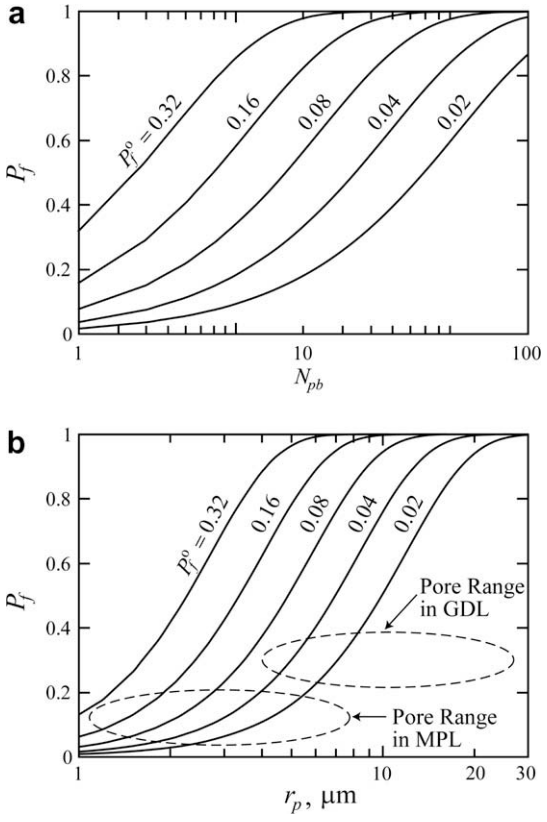

Fig. 7. Flooding probability P_f for pores in GDL at CL–GDL interface: (a) for pores connected with N_{pb} potential breakthrough pores in CL, and (b) for circular pores with radius r_p (assuming $n_{pb,CL}$ = 1/9 μm^{-2}).

3.4. Effect of interfacial water droplets

3.4.1. Diffusion limitation in CL

Water droplets formed at GC generally deteriorate the diffusion rate by reducing the surface area for the convective mass transport at GDL–GC interface. Similarly, the interfacial water droplets formed at CL–GDL interface obstruct the gas diffusion into CL. Considering very fine structures and small effective diffusivities of CL, the negative impact of the interfacial droplets on cell performance can be significant. Although the loss of diffusivities in GDL or in CL, due to local water saturation, has been considered in many studies, the diffusion and reaction limitations in CL caused by these interfacial water droplets have not been addressed. Here, numerical simulations are conducted to clarify the effects of interfacial droplets at CL–GDL interface on the diffusion and electrochemical reaction in CL.

A simple geometrical model for the interfacial water droplets formed on surface of CL is shown in Fig. 9, where equal-sized hemispherical droplets with radius r_d were assumed to be located in a hexagonal lattice. In Fig. 9(a), the hexagonal calculation domain is substituted by a circular domain, resulting in a two-dimensional diffusion and reaction problems in cylindrical coordinate as shown in Fig. 9(b). The size of the calculation domain is R in the radial direction and L_{CL} in the axial direction. A given concentration of

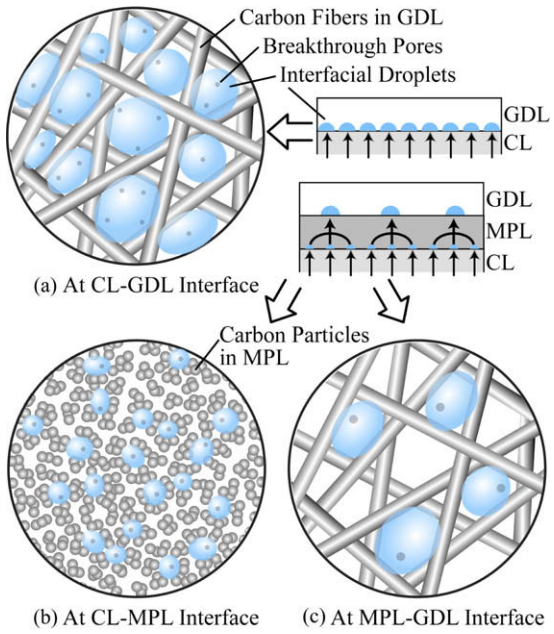

Fig. 8. Microscopic configuration of interfacial water droplets formed at (a) CL–GDL, (b) CL–MPL, and (c) MPL–GDL interfaces.

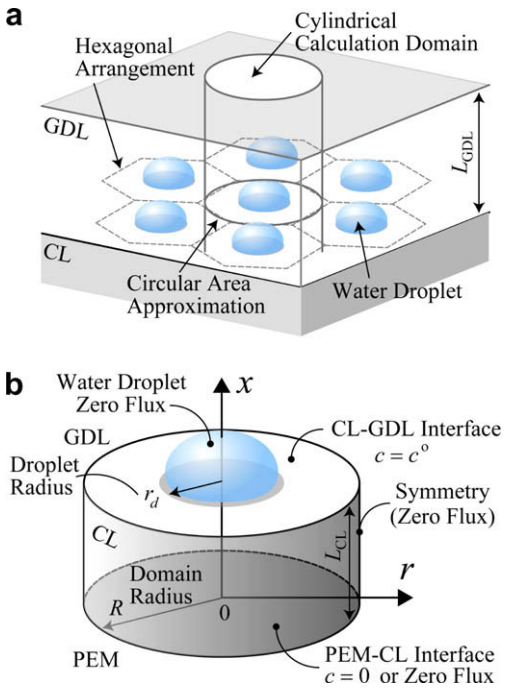

Fig. 9. Simplified geometric configuration for interfacial water droplets on surface of CL: (a) idealized droplet arrangement in a hexagonal lattice, and (b) a cylindrical geometry calculation domain for diffusion and reaction problems.

$c = c^o$ was imposed on a portion of the top surface which is not blocked (unshaded) by droplets, while a zero flux condition $\partial c/\partial x = 0$ is imposed on the other surfaces. For the pure diffusion problem, $c = 0$ is used on the bottom surface of CL, and the diffusion flux from the top open surface towards the bottom surface was calculated.

Two-dimensionless parameters were defined as

$$r_d^* = r_d/L_{CL}, \tag{13}$$

$$\alpha_d = \pi r_d^2/\pi R^2, \tag{14}$$

where r_d^* denotes relative radius of interfacial droplets, and α_d surface coverage ratio. The maximum diffusion flux in one-dimensional slab geometry without interfacial droplets is determined as

$$\dot{m}^o_{c,max} = M_c D_m \frac{c^o}{L_{CL}}, \tag{15}$$

where M_c denotes molar mass and D_m denotes the effective diffusivity in CL.

The maximum diffusion flux $\dot{m}_{c,max}$ with interfacial water droplets is plotted in Fig. 10 after normalized by $\dot{m}^o_{c,max}$ as $\dot{m}_{c,max}/\dot{m}^o_{c,max}$. It is observed that interfacial droplets on surface of CL hinder diffusion through CL, and this becomes more important when the surface coverage α_d or the relative droplet radius r_d^* increases. Recall that interfacial droplets at CL–MPL interface are much smaller than those at CL–GDL interface, as shown in Fig. 10(a) and (b). Inserting MPL can greatly reduce the diffusion limitation caused by droplets on surface of CL.

It may seem that $\alpha_d > 0.5$ is too high, however note that presence of solid matrix (pores) on surface of CL is ignored in this simulation. In Fig. 9, the surface coverage α_d only measures the area blocked by droplets, while the remaining area is available for diffusion. As illustrated in Fig. 8(a) and (b), the solid matrix blocks a considerable portion of CL surface and the interfacial droplets are preferentially formed in the pore space among solid obstacles. For example, the surface coverage α_d solely due to the solid structure is estimated from porosity as 0.4 for GDL and 0.5 for MPL. In addition, the length of blockage is estimated as 10 μm for GDL (from fiber size), and 1 μm for MPL (from particle size). Therefore, actual surface coverage α_d encountered at CL–GDL interface is very high as shown in Fig. 8(a).

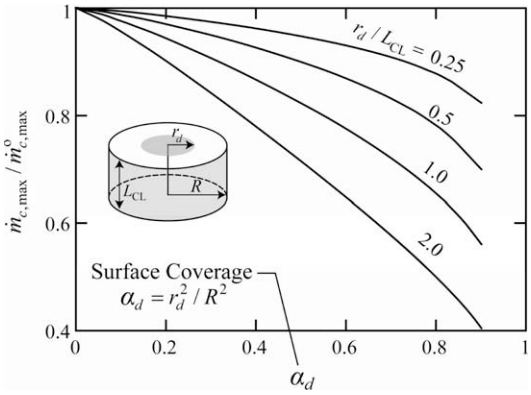

Fig. 10. Simulated effect of interfacial water droplets at CL–GDL interface on maximum diffusion rates in CL.

3.4.2. Reaction limitation in CL

The loss in the reaction rate caused by presence of interfacial droplets on surface of CL is examined by solving the diffusion-reaction problem. A zero flux condition of $\partial c/\partial x = 0$ is imposed at the bottom surface as shown in Fig. 9(b) and the volumetric consumption in CL is assumed proportional to reaction rate $\dot{n}$. The catalyst effectiveness factor η_{eff} is used as a measure of activity loss in porous media (caused by mass transport limitations). For a first-order reaction $\dot{n} = -kM_c c$, the effectiveness factor for a one-dimensional slab geometry η^o_{eff} is analytically given as [50]

$$\eta^o_{eff} = \frac{\tanh \Phi}{\Phi}. \tag{16}$$

Here, Φ is Thiele modulus defined as ratio of diffusion time to reaction time,

$$\Phi = L_{CL}\left(\frac{k}{D_m}\right)^{1/2}, \tag{17}$$

and k denotes the reaction rate coefficient.

Fig. 11(a) shows three concentration profiles in CL without interfacial droplets (same as a one-dimensional slab geometry) for $\Phi = 1$, 2, and 3. Higher Φ results in lower concentration and lower effectiveness factor, since reaction is limited by diffusion as Φ increases. The normalized effectiveness factor η_{eff}/η^o_{eff}, with interfacial droplets on surface of CL, is shown in Fig. 11(b) and (c) and the results indicate that the interfacial droplets significantly deteriorate the effectiveness factor in CL (similar to the results in Fig. 10). It is also observed that reduction in effectiveness factor is more noticeable when concentration in CL decreases according to increase in α_d, r_d^* or Φ. Fig. 11(b) and (c) also show that loss in effectiveness factor for $r_d^* = 2$ is proportional to α_d, indicating that diffusion rate governs the reaction rates.

3.4.3. Electrochemical limitation in CL

Effect of interfacial droplets on electrochemical reaction in CL is examined by solving fuel cell equations for the cathode half-cell geometry shown in Fig. 12. Different from the previous geometric model shown in Fig. 9, GDL and CL–GDL interface were included in the calculation domain. The shaded portion at center is assumed blocked, while the remaining CL–GDL interface is open. The volume of droplets in GDL was not considered in the simulation. Electronic and ionic potentials, electrochemical reaction rate, and oxygen concentration were selected as main variables, while tem-

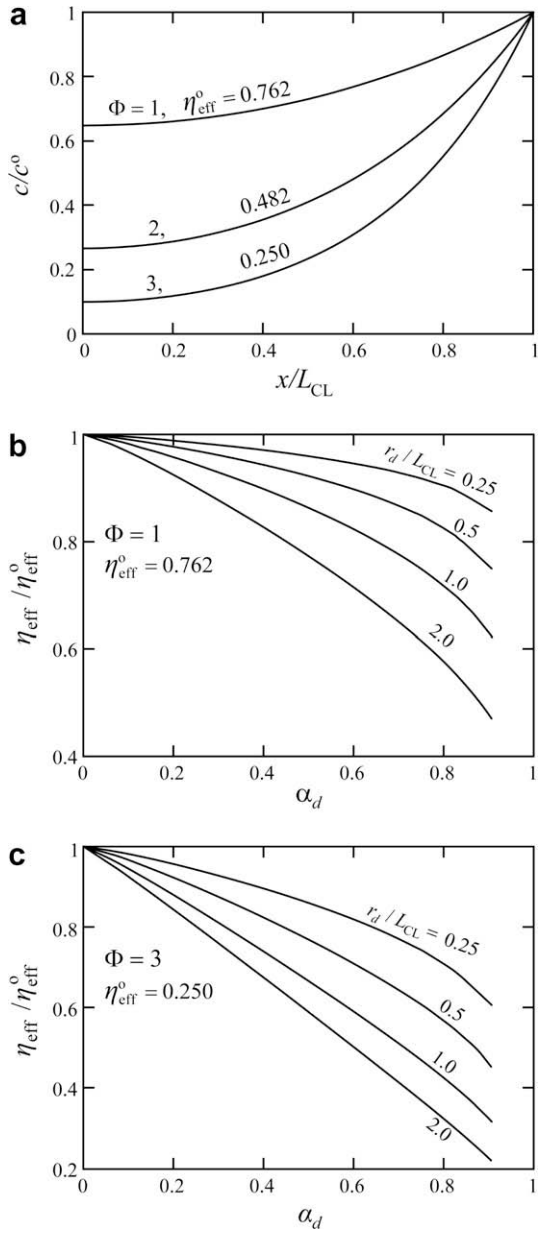

Fig. 11. Simulated effect of interfacial water droplet at CL–GDL interface on first-order reaction rates in CL: (a) concentration profiles for slab geometries, and relative effectiveness factors for (b) $\Phi = 1$ and (c) $\Phi = 3$.

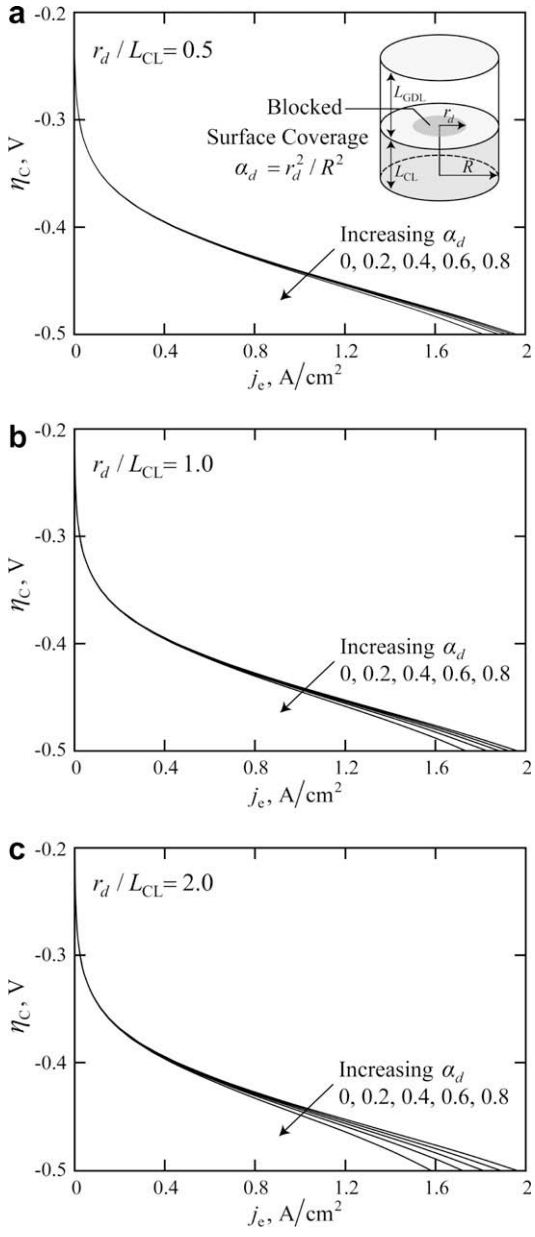

Fig. 12. Simulated effect of interfacial water droplet at CL–GDL interface on electrochemical reaction rates in CL: overpotential versus current density curves for (a) $r_d/L_{CL} = 0.5$, (b) $r_d/L_{CL} = 1.0$, and (c) $r_d/L_{CL} = 2.0$.

perature and vapor pressure were set constant by assuming an isothermal and fully-saturated condition. For direct comparison of effect of interfacial droplets, a constant average saturation was assumed for CL and GDL.

The properties and operating conditions are summarized in Table 2. The effective diffusivity of oxygen in GDL ($\varepsilon_{GDL} = 0.6,\ \bar{s}_{GDL} = 0.3$) is obtained from [23,51]

$$D^{eff}_{O_2,GDL} = D_{O_2}\varepsilon_{GDL}\left(\frac{\varepsilon_{GDL} - 0.11}{1 - 0.11}\right)^{0.785}(1 - \bar{s}_{GDL})^2, \tag{18}$$

where D_{O_2} is the effective diffusivity of oxygen in plain medium, estimated to be about 29 mm^2/s by considering multi-component diffusion in fully-saturated air at 70 °C and 1 atm. Similarly, the effective diffusivity of oxygen in CL ($\varepsilon_{CL} = 0.25,\ \bar{s}_{CL} = 0.4$) is obtained as

$$D^{eff}_{O_2,CL} = D_{O_2}[\varepsilon_{CL}(1 - \bar{s}_{CL})]^{1.5}k(\bar{d}_{p,CL}). \tag{19}$$

Here, $[\varepsilon_{CL}(1 - \bar{s}_{CL})]^{1.5}$ term accounts for effect of void volume reduction due to liquid water saturation, based on effective medium theory. The additional effect of water saturation in CL, i.e., pore size affecting gas diffusion, was considered by adopting the Knudsen factor $k(\bar{d}_{p,CL})$ proposed in [52]. The liquid saturation $\bar{s}_{CL}$ of 0.4 was estimated based on the measured hydrophilic pore fractions [49]. At this saturation level, most of large pores in CL are flooded by liquid water, and the mean radius of unflooded pores which participate in gas diffusion becomes smaller than $\bar{r}_{p,CL}$. Here, $k(\bar{d}_{p,CL})$ is set 0.35 [52] by assuming $\bar{d}_{p,CL} = 0.1$ μm.

The oxygen mole concentration in GC $c_{O_2,\infty}$ was set to be 0.75×5.16 mol/m^3, which corresponds to 50% utilization of fully-humidified air (at 70 °C, 1 atm) in cathodes. The mass transfer coefficient at GDL–GC interface h_{m,O_2} is estimated based on Sherwood number of 2.693 [21] and a channel height of 1 mm. The rate

Table 2
Properties and operating conditions for cathode overpotential simulations.

Properties	Values or expressions
Temperature T	70 °C
Pressure p	1 atm
Oxygen concentration $c_{O_2,\infty}$	0.75×5.16 mol/m^3
Mass transfer coefficient h_{m,O_2}	0.078 m/s
GDL	
Thickness L_{GDL}	250 μm
Effective diffusivity $D^{eff}_{O_2,GDL}$	5.3 mm^2/s
Electrical conductivity $\sigma_{e,GDL}$	1000 S/m
CL	
Thickness L_{CL}	10 μm
Effective diffusivity $D^{eff}_{O_2,CL}$	0.59 mm^2/s
Electrical conductivity $\sigma_{e,CL}$	500 S/m
Ionic conductivity $\sigma_{H^+,CL}$	2.0 S/m
Cathode reaction	
Transfer current j_C	$j_C = -a^{ref}_{o,C}\left(\frac{c_{O_2}}{c_{O_2,ref}}\right)\exp\left(-\frac{\alpha_C F}{RT}\eta_C\right)$ A/m^3
Volumetric exchange current density $aj^{ref}_{o,C}$	10,000 A/m^3
Reference oxygen concentration $c_{O_2,ref}$	40.88 mol/m^3
Transfer coefficient α_C	1

equation for cathode electrochemical reactions was adopted from [27].

Fig. 12 shows variation of current density versus cathodic overpotential, j_e–η_C. It is observed that current generation in cathodes deteriorates with increase in α_d and r^*_d. Thus, Fig. 12 clearly demonstrates the advantage of using MPL, because the size and the saturation level of interfacial droplets is generally larger on CL–GDL interface than on CL–MPL interface. Fig. 12 also indicates that the limiting effect of interfacial droplets on cell performance becomes more conspicuous at higher current densities. This trend is consistent with many experimental results showing MPL enhances cell performances at higher current densities, but do not noticeably so at lower current densities. This is because primary role of MPL is relative to mass transport processes, and the mass transport rates in PTL become limiting at higher current densities or low oxygen concentrations.

3.5. Water saturation in PTL

3.5.1. Water transport in MPL

The water transport in MPL is similar to that in GDL. Assuming liquid phase production of water or attainment of local thermodynamic equilibrium in CL, there is less volumetric generation of liquid by condensation inside MPL. The continuum two-phase flow models developed for GDL are in fact more proper for MPL which are naturally isotropic and homogeneous particulate media. The continuity of capillary pressure is still difficult to achieve at CL–MPL and MPL–GDL interface, due to the considerable difference in pore size across those interfaces (see Table 1). Thus, the saturation at MPL side of MPL–GDL interface s_{M-D^-} is dependent only on the pore structure of MPL and liquid flux $\dot{m}_l$ as

$$s_{M-D^-} = f(\dot{m}_l) = s_{im,MPL} + \beta_{MPL}\dot{m}_l, \tag{20}$$

where β_{MPL} is small, similar to β_{GDL}. The saturation level at MPL side of CL–MPL interface s_{C-M^+} may be estimated by referring to pore-size distribution of MPL with aid of Eq. (12) or Fig. 7(b).

The microscopic behavior of liquid in GDL is similar to MPL. Liquid in MPL preferentially invades large pores through invasion-percolation process, and many transport paths near CL–MPL interface are merged into a small number of breakthrough pores at MPL–GDL interface. Thus, the minimum number density of breakthrough pores from MPL is estimated similar to Eq. (8) as

$$N^{min}_{b,MPL} = \frac{1}{\pi L^2_{MPL}}. \tag{21}$$

For MPL with L_{MPL} = 50 μm, $N^{min}_{b,MPL} = 130$ breakthrough pores per mm^2. Note that $n_{b,CL}$ was estimated as 4500 breakthrough pores per mm^2 for 4% flooding probability ($P^o_f = 0.04$). Thus, inserting MPL between CL and GDL significantly reduces the number of breakthrough pores toward GDL. The saturation level of interfacial droplets formed at MPL–GDL interface is small, as illustrated in Fig. 8(c).

The second role of MPL in water management of PEMFC is identified to reduce the number density of breakthrough pores towards GDL by efficiently collecting uniform liquid water flux from CL. The consequence of this role of MPL is also depicted in Figs. 2(b) and 8(c). Note that MPL cannot directly influence the water transport in CL located upstream, due to a large difference in the capillary pressure between CL and MPL. However, MPL can modify the electrochemical reaction in CL by changing the interfacial condition on surface of CL. In addition, MPL can directly influence water transport in GDL located downstream by changing the source side-condition towards GDL as explained below.

3.5.2. Saturation distribution in PTL

The water saturation distribution in GDL for a constant liquid flux is shown in Fig. 13(a), predicted by continuum two-phase flow models [5,21–27,41]. The peculiarity of the continuum models is that they do not require the source-side saturation as a boundary condition. Instead, a given liquid flux condition is generally prescribed at CL–GDL interface. Then, the saturation distribution is obtained by integrating Eq. (5) backward using the predetermined liquid flux $\dot{m}_l$, starting from an immobile saturation $s_{im,GDL}$ at GDL–GC interface toward CL–GDL interface. As a result, the saturation at CL–GDL interface $s^{min}_{C-D^+}$ is determined as shown in Fig. 13(a).

The properties used in the continuum models are macroscopic ones which are generally evaluated during two-phase drainage experiments. In those experiments, liquid water is transported through hydrophobic GDL by increasing the liquid pressure on one side while maintaining the gas pressure on the other side. Thus, largest pores in GDL are preferentially used for the liquid flow while smaller pores do not participate in the liquid transport. It is pointed out in [30] that the source-side condition encountered at CL–GDL interface in operating cell is quite different from the above condition (a uniform inlet pressure condition). Liquid water from CL intrudes the pores in GDL, similar to injected by small needles (a uniform inlet flux condition) as shown in Fig. 4, and thus smaller pores in the GDL are also flooded although their flooding probabilities may be small. The liquid water introduced into such smaller pores should also find paths for its transport, and this generally results in higher saturation levels than predicted by the continuum models. Therefore, the saturation distribution predicted by continuum two-phase flow models should be viewed as a statistical minimum saturation required for the steady flow of the given liquid water flux through GDL. Thus $s^{min}_{C-D^+}$ is the minimum saturation observable at CL–GDL interface.

The saturation level of interfacial droplets formed at CL–GDL interface or MPL–GDL interface depend on the number density of breakthrough pores toward GDL and the pore size distribution in GDL. Thus, the actual saturation at GDL side of CL–GDL interface s_{C-D^+} is larger than $s^{min}_{C-D^+}$, as shown in Figs. 7 and 8, while that at MPL–GDL interface s_{M-D^+} may be similar to or smaller than $s^{min}_{C-D^+}$. Two saturation distributions in GDL for $s_{C-D^+} > s^{min}_{C-D^+}$ are presented in Fig. 13(a) as profiles A and B. Profile A assumes that the source-side condition globally influences the saturation distribution in GDL, significantly increasing the saturation level. However, profile B assumes that the liquid transport readily approaches that predicted by the continuum models after small deviation near

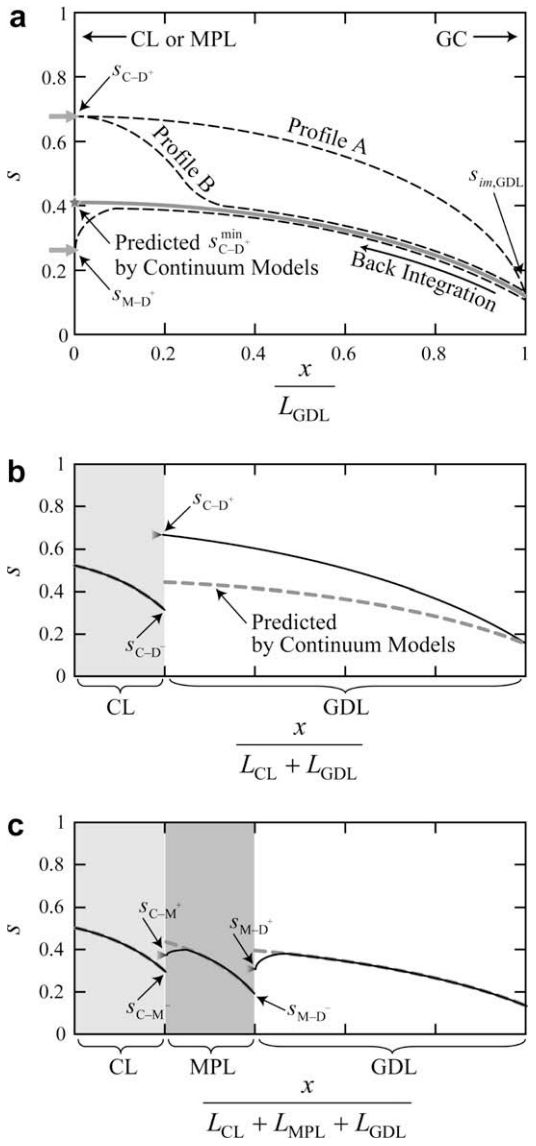

Fig. 13. Proposed water saturation distributions in (a) GDL, (b) CL + GDL construction, and (c) CL + MPL + GDL construction.

CL–GDL interface. Recent pore-network analysis in [30] suggests that the profile A is more plausible, because the transport paths developed by uniform liquid flux from CL cannot easily merge while flowing through a relatively thin GDL (compared with its mean pore radius). The saturation distribution in GDL for $s_{C-D^+} < s_{C-D^+}^{min}$ is also proposed in Fig. 13(a). If the continuum two-phase flow models properly predict the minimum saturation distribution required for transporting given liquid flux, the accumulation of liquid in GDL continues till the steady minimum saturation is met.

The saturation distribution in a cathode with CL + GDL and one with CL + MPL + GDL are proposed in Fig. 13(b) and (c). Note that the saturation jumps at the CL–GDL, CL–MPL, and MPL–GDL interfaces shown in Fig. 13 are not the results of the continuous capillary pressure at those interfaces [23,24]. Instead, each saturation jump is caused by the difference between the immobile saturation of the upstream fine medium and the saturation level of interfacial droplets formed at downstream coarse medium. By insertion of MPL, the interfacial saturation on surface of CL is reduced from s_{C-D^+} in Fig. 13(b) to a smaller s_{C-M^+} in Fig. 13(c), and also the interfacial saturation level toward GDL is reduced from s_{C-D^+} in Fig. 13(b) to a smaller s_{M-D^+} in Fig. 13(c). The reduced saturation level on surface of CL enhances electrochemical activities of CL as demonstrated from Figs. 10–12. And the reduced source-side saturation toward GDL decreases the saturation level in GDL as explained in Fig. 13(a).

Note that the saturation distribution in CL of Fig. 13(c) is drawn unaffected by insertion of MPL. However, the saturation in CL can be reduced by inserting MPL between CL and GDL. This is because production and transport process in CL become more unstable when interfacial droplets on surface of CL can grow very large, similar to the discussion at the end of Section 3.3.2. Consider a certain region of CL which is more electrochemically active, generating more water than the remaining regions. Then, the surface pores in that region will have higher flooding probabilities, and thus that region is more prone to be covered by interfacial droplets. If the droplet can grow large enough to significantly reduce the current generation in that region, more current should be produced in other regions of CL, preferentially with less interfacial droplets. More current generation in those regions leads to more water generation, and in turn increases the flooding probabilities of the surface pores there. Eventually, large interfacial droplets will grow and cover those regions and even more current should be produced in still other regions of CL. By inserting MPL, the size of the interfacial droplets on surface of CL is controlled and this gradual degradation phenomenon is avoided.

4. Discussion

It is generally accepted that MPL should provide higher hydrophobicity and smaller pore size compared with GDL, in order to reduce electrode flooding failures. It is also believed that the bi-modal pore size distributions in MPL are favorable for the performance of PEMFC by facilitating the separation of water-transporting paths and gas-diffusing paths [15–18]. According to the proposed model, MPL should provide smaller surface pore sizes at CL–MPL interface. This is because the size of interfacial droplets formed on surface of CL is determined primarily by those surface pores in MPL, as pointed in [7]. Smaller pores in MPL at CL–MPL interface prevent interfacial droplets from growing very large. In addition, smaller pores also act as compartments which reduce the saturation level at CL–MPL interface, as shown in Fig. 8. This explanation is consistent with recent experiment showing an improved performance of a PEMFC using a porosity-graded MPL [20]. Lower porosity, smaller particle size, or higher hydrophobicity on CL side in graded MPL reduces the surface pore size there, which in turn enhances electrochemical reactions by reducing the size and saturation level of interfacial droplets on surface of CL.

The present model also predicts that there is an optimal thickness for MPL. Many experiments showed that optimal cell performance when thickness of MPL is about 50 μm [8,12–14]. Previously, this was explained based on an enhanced electrical contact between CL and MPL offered by thick MPL. However, an alternative explanation is given by our proposed model. As discussed in relation to Eq. (19), the breakthrough number density at MPL–GDL interface is a function of MPL thickness. If the thickness is small, MPL cannot efficiently collect the water from CL, resulting in smaller reduction in number density of liquid water breakthroughs toward GDL. That is, a thin MPL only shift the position of large interfacial droplets along the MPL thickness (from surface of CL to surface of thin MPL) while not changing their size and saturation level significantly.

In summary, an optimized MPL should provide a small surface pore size in CL side of the MPL which can efficiently confine interfacial droplets formed on surface of CL to reduce their size and saturation level. In addition it should also provide a pore structure in the remaining part of MPL which can efficiently merge many trans-

port paths formed by liquid water breakthrough from CL in order to reduce the liquid water breakthrough toward GDL.

5. Summary

Two roles of MPL in water morphology control in PEMFC are proposed. First, MPL inserted between CL and GDL reduces the size and the saturation level of interfacial water droplets formed on CL surface; this increases the diffusion rate into CL, enhancing electrochemical reactions in CL. Second, MPL reduces the number of liquid water breakthroughs toward GDL; this decreases the liquid water saturations in GDL, enhancing oxygen diffusion. Based on the proposed physical model, the structural requirements of MPL for better PEMFC performances are discussed. MPL should provide small pore size toward the CL side to reduce the size and saturation level of interfacial water droplets. At the same time, it should efficiently collect the liquid water from CL, thus reducing the number of liquid water breakthroughs toward GDL.

References

[1] J. Larminie, A. Dicks, Fuel Cell Systems Explained, Wiley, Chichester, 2000.
[2] S. Litster, G. McLean, PEM fuel cell electrodes, J. Power Sources 130 (2004) 61–76.
[3] A.Z. Weber, J. Newman, Modeling transport in polymer–electrolyte fuel cells, Chem. Rev. 104 (2004) 4679–4726.
[4] C.Y. Wang, Fundamental models for fuel cell engineering, Chem. Rev. 104 (2004) 4727–4765.
[5] W.S. He, J.S. Yi, T.V. Nguyen, Two-phase flow model of the cathode of PEM fuel cells using interdigitated flow fields, AIChE J. 46 (2000) 2053–2064.
[6] S. Dutta, S. Shimpalee, J.W. Van Zee, Numerical prediction of mass-exchange between cathode and anode channels in a PEM fuel cell, Int. J. Heat Mass Transfer 44 (2001) 2029–2042.
[7] M.S. Wilson, J.A. Valerio, S. Gottesfeld, Low platinum loading electrodes for polymer electrolyte fuel cells fabricated using thermoplastic ionomers, Electrochim. Acta 40 (1995) 355–363.
[8] V.A. Paganin, E.A. Ticianelli, E.R. Gonzalez, Development and electrochemical studies of gas diffusion electrodes for polymer electrolyte fuel cells, J. Appl. Electrochem. 26 (1996) 297–304.
[9] L. Giorgi, E. Antolini, A. Pozio, E. Passalacqua, Influence of the PTFE content in the diffusion layer of low-Pt loading electrodes for polymer electrolyte fuel cells, Electrochim. Acta 43 (1998) 3675–3680.
[10] L.R. Jordan, A.K. Shukla, T. Behrsing, N.R. Avery, B.C. Muddle, M. Forsyth, Diffusion layer parameters influencing optimal fuel cell performance, J. Power Sources 86 (2000) 250–254.
[11] Z. Qi, A. Kaufman, Improvement of water management by a microporous sublayer for PEM fuel cells, J. Power Sources 109 (2002) 38–46.
[12] J.M. Song, S.Y. Cha, W.M. Lee, Optimal composition of polymer electrolyte fuel cell electrodes determined by the AC impedance method, J. Power Sources 94 (2001) 78–84.
[13] H.K. Lee, J.H. Park, D.Y. Kim, T.H. Lee, A study on the characteristics of the diffusion layer thickness and porosity of the PEMFC, J. Power Sources 131 (2004) 200–206.
[14] C.J. Tseng, S.K. Lou, Y.Y. Yan, L.Y. Sung, Gas diffusion layer and microporous layer for PEMFC, in: Proceedings of the International Hydrogen Energy Congress and Exhibition (IHEC 2005), Istanbul, Turkey, 13–15 July 2005.
[15] C.S. Kong, D.Y. Kim, H.K. Lee, Y.G. Shul, T.H. Lee, Influence of pore-size distribution of diffusion layer on mass-transport problems of proton exchange membrane fuel cells, J. Power Sources 108 (2002) 185–191.
[16] X.L. Wang, H.M. Zhang, J.L. Zhang, H.F. Xu, Z.Q. Tian, J. Chen, H.X. Zhong, Y.M. Liang, B.L. Yi, Micro-porous layer with composite carbon black for PEM fuel cells, Electrochim. Acta 51 (2006) 4909–4915.
[17] X.L. Wang, H.M. Zhang, J.L. Zhang, H.F. Xu, X.B. Zhu, J. Chen, B.L. Yi, A bi-functional micro-porous layer with composite carbon black for PEM fuel cells, J. Power Sources 162 (2006) 474–479.
[18] G.G. Park, Y.J. Sohn, S.D. Yim, T.H. Yang, Y.G. Yoon, W.Y. Lee, K. Eguchi, C.S. Kim, Adoption of nano-materials for the micro-layer in gas diffusion layers of PEMFCs, J. Power Sources 163 (2006) 113–118.
[19] S. Park, J.W. Lee, B.N. Popov, Effect of carbon loading in microporous layer on PEM fuel cell performance, J. Power Sources 163 (2006) 357–363.
[20] H.L. Tang, S.L. Wang, M. Pan, R.Z. Yuan, Porosity-graded micro-porous layers for polymer electrolyte membrane fuel cells, J. Power Sources 166 (2007) 41–46.
[21] Z.H. Wang, C.Y. Wang, K.S. Chen, Two-phase flow and transport in the air cathode of proton exchange membrane fuel cells, J. Power Sources 94 (2001) 40–50.
[22] L.X. You, H.T. Liu, A two-phase flow and transport model for the cathode of PEM fuel cells, Int. J. Heat Mass Transfer 45 (2002) 2277–2287.
[23] J.H. Nam, M. Kaviany, Effective diffusivity and water-saturation distribution in single- and two-layer PEMFC diffusion medium, Int. J. Heat Mass Transfer 46 (2003) 4595–4611.
[24] U. Pasaogullari, C.Y. Wang, Two-phase transport and the role of micro-porous layer in polymer electrolyte fuel cells, Electrochim. Acta 49 (2004) 4359–4369.
[25] A.Z. Weber, J. Newman, Effects of microporous layers in polymer electrolyte fuel cells, J. Electrochem. Soc. 152 (2005) A677–A688.
[26] G.Y. Lin, T.V. Nguyen, A two-dimensional two-phase model of a PEM fuel cell, J. Electrochem. Soc. 153 (2006) A372–A382.
[27] Y. Wang, C.Y. Wang, A non-isothermal two-phase model for polymer electrolyte fuel cells, J. Electrochem. Soc. 153 (2006) A1193–A1200.
[28] K. Karan, H.K. Atiyeh, A. Phoenix, E. Halliop, J. Pharoah, B. Peppley, An experimental investigation of water transport in PEMFCs – the role of microporous layers, Electrochem. Solid State Lett. 10 (2007) B34–B38.
[29] H.K. Atiyeh, K. Karan, B. Peppley, A. Phoenix, E. Halliop, J. Pharoah, Experimental investigation of the role of a microporous layer on the water transport and performance of a PEM fuel cell, J. Power Sources 170 (2007) 111–121.
[30] K.J. Lee, J.H. Nam, C.J. Kim, Pore-network analysis of two-phase water transport in gas diffusion layers of polymer electrolyte membrane fuel cells, Electrochim. Acta 54 (2009) 1166–1176.
[31] H.M. Yu, J.O. Schumacher, M. Zobel, C. Hebling, Analysis of membrane electrode assembly (MEA) by environmental scanning electron microscope (ESEM), J. Power Sources 145 (2005) 216–222.
[32] F.Y. Zhang, D. Spernjak, A.K. Prasad, S.G. Advani, In situ characterization of the catalyst layer in a polymer electrolyte membrane fuel cell, J. Electrochem. Soc. 154 (2007) B1152–B1157.
[33] M.V. Williams, E. Begg, L. Bonville, H.R. Kunz, J.M. Fenton, Characterization of gas diffusion layers for PEMFC, J. Electrochem. Soc. 151 (2004) A1173–A1180.
[34] M. Khandelwal, M.M. Mench, Direct measurement of through-plane thermal conductivity and contact resistance in fuel cell materials, J. Power Sources 161 (2006) 1106–1115.
[35] J.G. Pharoah, K. Karan, W. Sun, On effective transport coefficients in PEM fuel cell electrodes: anisotropy of the porous transport layers, J. Power Sources 161 (2006) 214–224.
[36] J.T. Gostick, M.W. Fowler, M.D. Pritzker, M.A. Ioannidis, L.M. Behra, In-plane and through-plane gas permeability of carbon fiber electrode backing layers, J. Power Sources 162 (2006) 228–238.
[37] J.P. Feser, A.K. Prasad, S.G. Advani, Experimental characterization of in-plane permeability of gas diffusion layers, J. Power Sources 162 (2006) 1226–1231.
[38] K. Broka, P. Ekdunge, Modelling the PEM fuel cell cathode, J. Appl. Electrochem. 27 (1997) 281–289.
[39] N.P. Siegel, M.W. Ellis, D.J. Nelson, M.R. Spakovsky, Single domain PEMFC model based on agglomerate catalyst geometry, J. Power Sources 115 (2003) 81–89.
[40] W. Sun, B.A. Peppley, K. Karan, An improved two-dimensional agglomerate cathode model to study the influence of catalyst layer structural parameters, Electrochim. Acta 50 (2005) 3359–3374.
[41] C. Ziegler, H.M. Yu, J.O. Schumacher, Two-phase dynamic modeling of PEMFCs and simulation of cyclo-voltammograms, J. Electrochem. Soc. 152 (2005) A1555–A1567.
[42] M. Karviany, Principles of Heat Transfer in Porous Media, second ed., Springer, New York, 1999.
[43] P.K. Sinha, C.Y. Wang, Pore-network modeling of liquid water transport in gas diffusion layer of a polymer electrolyte fuel cell, Electrochim. Acta 52 (2007) 7936–7945.
[44] S. Litster, D. Sinton, N. Djilali, Ex situ visualization of liquid water transport in PEM fuel cell gas diffusion layers, J. Power Sources 154 (2006) 95–105.
[45] A. Bazylak, D. Sinton, Z.S. Liu, N. Djilali, Effect of compression on liquid water transport and microstructure of PEMFC gas diffusion layers, J. Power Sources 163 (2007) 784–792.
[46] F.Y. Zhang, X.G. Yang, C.Y. Wang, Liquid water removal from a polymer electrolyte fuel cell, J. Electrochem. Soc. 153 (2006) A225–A232.
[47] H.M. Yu, C. Ziegler, M. Oszcipok, M. Zobel, C. Hebling, Hydrophilicity and hydrophobicity study of catalyst layers in proton exchange membrane fuel cells, Electrochim. Acta 51 (2006) 1199–1207.
[48] J.T. Gostick, M.W. Fowler, M.A. Ioannidis, M.D. Pritzker, Y.M. Volfkovich, A. Sakars, Capillary pressure and hydrophilic porosity in gas diffusion layers for polymer electrolyte fuel cells, J. Power Sources 156 (2006) 375–387.
[49] Q. Ye, T.V. Nguyen, Three-dimensional simulation of liquid water distribution in a PEMFC with experimentally measured capillary functions, J. Electrochem. Soc. 154 (2007) B1242–B1251.
[50] R.B. Bird, W.E. Stewart, E.N. Lightfoot, Transport Phenomena, second ed., Wiley, New York, 2002.
[51] M.M. Tomadakis, S.V. Sotirchos, Ordinary and transition regime diffusion in random fiber structures, AIChE J. 39 (1993) 397–412.
[52] D. Mu, Z.S. Liu, C. Huang, N. Djilali, Determination of the effective diffusion coefficient in porous media including Knudsen effects, Microfluid Nanofluid 4 (2008) 257–260.